JM PAPERS

Multistability of elasto-inertial two-dimensional channel flow

Miguel Beneitez[1],†, Jacob Page[2], Yves Dubief[3] and Rich R. Kerswell[1]

[1]DAMTP, Centre for Mathematical Sciences, Wilberforce Road, Cambridge CB3 0WA, UK

[2]School of Mathematics, University of Edinburgh, Edinburgh EH9 3FD, UK

[3]Department of Mechanical Engineering, University of Vermont, Burlington, VT 05405, USA

Elasto-inertial turbulence (EIT) is a recently discovered two-dimensional chaotic flow state observed in dilute polymer solutions. Two possibilities are currently hypothesized to be linked to the dynamical origins of EIT: (i) viscoelastic Tollmien–Schlichting waves and (ii) a centre-mode instability. The nonlinear evolution of the centre mode leads to a travelling wave with an 'arrowhead' structure in the polymer conformation, a structure also observed instantaneously in simulations of EIT. In this work we conduct a suite of two-dimensional direct numerical simulations spanning a wide range of polymeric flow parameters to examine the possible dynamical connection between the arrowhead and EIT. Our calculations reveal (up to) four coexistent attractors: the laminar state and a steady arrowhead regime (SAR), along with EIT and a 'chaotic arrowhead regime' (CAR). The SAR is stable for all parameters considered here, while the final pair of (chaotic) flow states are visually very similar and can be distinguished only by the presence of a weak polymer arrowhead structure in the CAR regime. Analysis of energy transfers between the flow and the polymer indicates that both chaotic regimes are maintained by an identical near-wall mechanism and that the weak arrowhead does not play a role. Our results suggest that the arrowhead is a benign flow structure that is disconnected from the self-sustaining mechanics of EIT.

Key words: transition to turbulence, viscoelasticity

1. Introduction

It has been more than 70 years since the phenomenon of polymer drag reduction in wall-bounded turbulence was first observed experimentally (Toms 1948; Mysels 1949). Following this discovery, great efforts have been directed towards understanding

† Email address for correspondence: mb2467@cam.ac.uk

how inertial turbulence (IT) is altered by the addition of polymers to the flow (e.g. see the reviews Lumley 1969; White & Mungal 2008). Polymeric fluids also exhibit counter-intuitive chaotic behaviour in very small-scale, inertialess flows. This 'elastic' turbulence (ET) was also first discovered experimentally (Groisman & Steinberg 2000, 2004) at vanishing Reynolds numbers and is thought to rely on finite-amplitude curvature in the streamlines (Shaqfeh 1996). In contrast to polymer-modified IT, ET is associated with an increased drag relative to the laminar Newtonian state (Varshney & Steinberg 2018). It can be exploited to promote heat transfer (Traore, Castelain & Burghelea 2015) and to efficiently mix at very small scales (Squires & Quake 2005).

In addition to these distinct phenomena, a third chaotic flow state was recently identified (Dubief, Terrapon & Soria 2013; Samanta *et al.* 2013) where both inertial and elastic effects are relevant, and was named 'elasto-inertial' turbulence (EIT). Elasto-inertial turbulence can be sustained for Reynolds numbers $Re = O(1000)$, and is potentially linked to the 'early turbulence' reported in a range of experimental studies (Jones & Maddock 1966; Goldstein, Adrian & Kreid 1969; Draad, Kuiken & Nieuwstadt 1998; Chandra, Shankar & Das 2018; Choueiri, Lopez & Hof 2018). Elasto-inertial turbulence differs from both IT and ET in that it can be sustained in a purely two-dimensional planar flow (Sid, Terrapon & Dubief 2018), and is dominated by highly extended 'sheets' of polymer stress (see, e.g. Dubief, Terrapon & Hof 2023). A connection has been sought between EIT and the so-called 'maximum drag reduction' state in IT (Zhang *et al.* 2021; Zhu & Xi 2021), though the mechanisms underpinning both of these flow types remain to be clarified.

Despite much progress in our statistical understanding of the various chaotic viscoleastic flows (Datta *et al.* 2022; Sánchez *et al.* 2022; Dubief *et al.* 2023), the dynamical origins and connections between polymer-perturbed IT, EIT and ET remain largely unknown. The exception here is ET in curved geometries, which is associated with a linear instability driven by viscoelastic hoop stresses (Larson, Shaqfeh & Muller 1990; Shaqfeh 1996). In parallel flows there has been some indication that self-sustaining ET can be triggered by a finite-amplitude perturbation to generate the curvature necessary for a hoop-stress instability (Meulenbroek *et al.* 2004; Morozov & van Saarloos 2007; Pan *et al.* 2013), but the exact requirements and dynamical connection to the linear instabilities in a curved geometry has not been demonstrated and there is also the possibility of a direct connection to EIT.

The situation in a planar pressure-driven channel flow is ripe for investigation due to the presence of a pair of linear instabilities. One is the viscoelastic analogue of the Newtonian Tollmien–Schlichting (TS) waves and exists at high Re (Zhang *et al.* 2013). It has been observed that the polymer conformation field associated with a saturated TS wave and the polymer conformation for the weakly chaotic edge state for (subcritical) EIT have a similar appearance (Shekar *et al.* 2019, 2021) though the TS branch turns around prior to the emergence of EIT as the Weissenberg number Wi is increased and a clear dynamical connection has yet to be established. The other instability was discovered only very recently, and is a 'centre mode' found in both pipes (Garg *et al.* 2018) and channels (Khalid *et al.* 2021*a*) at modest Weissenberg numbers $Wi \sim 20$. Most intriguingly, the unstable centre mode in a channel remains unstable even in the inertialess limit (Khalid, Shankar & Subramanian 2021*b*), although only for very high Wi and vanishing polymer concentration (more realistic values of Wi are found with the introduction of a more realistic polymer model, see Buza, Page & Kerswell 2022*b*). The existence of a linear instability in areas of the parameter space relevant to both ET and EIT could provide a plausible direct connection between these states. The nonlinear evolution of the viscoelastic centre mode leads to a saturated 'arrowhead' travelling wave (Page,

Dubief & Kerswell 2020) that is strongly subcritical (Wan, Sun & Zhang 2021; Buza *et al.* 2022*b*). The arrowhead can be continued down to the inertialess limit where it is found to exist at experimentally realisable values of the Weissenberg number (Buza *et al.* 2022*a*; Morozov 2022). Finite-amplitude structures that are similar in appearance to the exact arrowhead travelling waves have been observed in experiments at low *Re* (Choueiri *et al.* 2021) and have also been seen intermittently in numerical simulations of EIT at high *Re* (Page *et al.* 2020; Dubief *et al.* 2022). However – much like the TS waves – a direct route to chaos from this structure (e.g. in a sequence of successive bifurcations) has yet to be found.

Although near-wall perturbations have been a signature of EIT since its discovery (Samanta *et al.* 2013), the possible importance of the arrowhead in sustaining EIT was suggested by the simulations of Dubief *et al.* (2022), who performed DNS of viscoelastic flows using the FENE-P model for $Re = 1000$, $Wi \in [50, 200]$ and $0.5 \le \beta \le 1$. Their study identified several regimes in different areas of the parameter space: a stable travelling wave arrowhead, EIT, a chaotic arrowhead regime (CAR) and an intermittent arrowhead regime. Motivated by these results, we conduct a systematic study of the state space of a two-dimensional viscoelastic channel flow for a wide range of polymeric parameters in the finite-extensibility nonlinear elastic-Peterlin (FENE-P) model, in an effort to directly connect the arrowhead to EIT. Surprisingly, we find that the arrowhead is a benign flow structure – it can be maintained on top of a background EIT, but does not play a role in the self-sustaining mechanism that is driven by near-wall behaviour. Our search reveals that the steady arrowhead structure travelling wave is always stable for the parameters we consider, and we also find a large region of multistability with up to four attractors – the laminar (L) state, SAR, EIT and CAR. The final regime is nearly identical to EIT apart from a weak arrowhead in the centre of the domain.

The rest of this paper is structured as follows. In § 2 we present the governing equations and describe the numerical simulations to be conducted. In § 3 we present evidence for the four distinct attractors and draw connections to the results of Dubief *et al.* (2022). In § 4 we look for dynamical connections between the attractors and compute various edge states between them. Finally, conclusions are presented in § 5.

2. Formulation and computational details

We consider a two-dimensional streamwise-periodic flow between two infinite, stationary, rigid walls, separated by a distance $2h$ and driven by a time-varying pressure gradient so that the mass flux is constant. The viscoelastic flow is governed by the FENE-P model with governing equations

$$\partial_t \boldsymbol{u} + (\boldsymbol{u} \cdot \nabla)\boldsymbol{u} + \nabla p = \frac{\beta}{Re}\Delta \boldsymbol{u} + \frac{(1-\beta)}{Re}\nabla \cdot \boldsymbol{T}(\boldsymbol{C}), \quad (2.1)$$

$$\partial_t \boldsymbol{C} + (\boldsymbol{u} \cdot \nabla)\boldsymbol{C} + \boldsymbol{T}(\boldsymbol{C}) = \boldsymbol{C} \cdot \nabla \boldsymbol{u} + (\nabla \boldsymbol{u})^{\mathrm{T}} \cdot \boldsymbol{C} + \frac{1}{Re\,Sc}\Delta \boldsymbol{C}, \quad (2.2)$$

$$\nabla \cdot \boldsymbol{u} = 0, \quad (2.3)$$

where

$$\boldsymbol{T}(\boldsymbol{C}) := \frac{1}{Wi}\left(f(\mathrm{tr}\boldsymbol{C})\boldsymbol{C} - \boldsymbol{I}\right), \quad \text{and} \quad f(x) := \left(1 - \frac{x-3}{L_{max}^2}\right)^{-1}. \quad (2.4a,b)$$

We consider two-dimensional flows with $\boldsymbol{u} = (u, v)$ denoting the streamwise and wall-normal velocity components, p the pressure and $\boldsymbol{C}$ the positive-definite conformation

tensor that represents the ensemble average of the product of the end-to-end vector of the polymer molecules. The parameter $\beta := \eta_s/(\eta_s + \eta_p)$ denotes the viscosity ratio, with η_s and η_p the solvent and polymer contributions to the total kinematic viscosity, $\eta = \eta_s + \eta_p$. The parameter L_{max} is the maximum extensibility of the polymer chains. The equations are made non-dimensional with the half-distance between the plates h and the bulk velocity

$$U_b := \frac{1}{2h} \int_{-h}^{h} u \, \mathrm{d}y. \tag{2.5}$$

The non-dimensional Reynolds, Re, and Weissenberg, Wi, numbers are defined as

$$Re := \frac{U_b h}{\eta} \quad \text{and} \quad Wi := \frac{\tau U_b}{h}, \tag{2.6a,b}$$

where τ denotes the polymer relaxation time. Equation (2.2) has a stress diffusion term that, for a realistic polymer solution, would take a value $Sc = O(10^6)$. However, numerical simulations are typically restricted to much smaller values, $Sc = O(10^3)$ (Sid *et al.* 2018; Page *et al.* 2020), and the term itself is treated as regulariser to help maintain positive-definite C. With non-zero polymer diffusion we must specify boundary conditions on the polymer conformation. As previously used in the literature (Page *et al.* 2020; Buza *et al.* 2022a; Dubief *et al.* 2022), we apply the following equation at the wall:

$$\partial_t C + T(C) = C \cdot \nabla u + (\nabla u)^{\mathrm{T}} \cdot C + \frac{1}{Re \, Sc} \partial_{xx} C. \tag{2.7}$$

Note that (2.2) does not require boundary conditions in the limit $Sc \to \infty$ (Sid *et al.* 2018); the boundary conditions (2.7) are chosen so that the distance from the $Sc \to \infty$ limit is minimized (Sid *et al.* 2018; Dubief *et al.* 2022).

2.1. *Numerics*

The spectral codebase Dedalus (Burns *et al.* 2020) is used to perform direct numerical simulations of (2.1)–(2.3). We consider a computational domain of fixed size $[L_x, L_y] = [2\pi, 2]$ in units of h. The quantities C and u are expanded in N_x Fourier modes in the x direction and N_y Chebyshev modes in the y direction. Time integration is performed with a third-order semi-implicit BDF scheme (Wang & Ruuth 2008) with a fixed time step. We fix $Sc = 500$ for the majority of simulations unless otherwise indicated. The different numerical solutions have various requirements in term of resolution. We typically use $[N_x, N_y] = [512, 600]$ to simulate travelling waves while higher values of $[N_x, N_y] = [600, 800]$ are used to simulate chaotic states, although for some of the higher Weissenberg and higher L_{max} cases, we have considered $[N_x, N_y] = [800, 1024]$. Further increasing Sc can cause C to lose positive definiteness in several locations of the domain, as previously reported by Dubief *et al.* (2022). However, reducing the computational time step and increasing the resolution can alleviate this. We have checked those results that temporarily lose positive definiteness in certain regions by reducing the time step below 10^{-5} and increasing the resolution to at least $[N_x, N_y] = [2048, 2048]$. The increase of spatio-temporal resolution ensured that positive definiteness is recovered while the reported dynamics remain unaltered.

2.2. *Elasto-inertial attractors*

Dubief *et al.* (2022) identified various statistically steady states in the same channel geometry: the L state, SAR, EIT and a CAR. Note that Dubief *et al.* (2022) also discuss
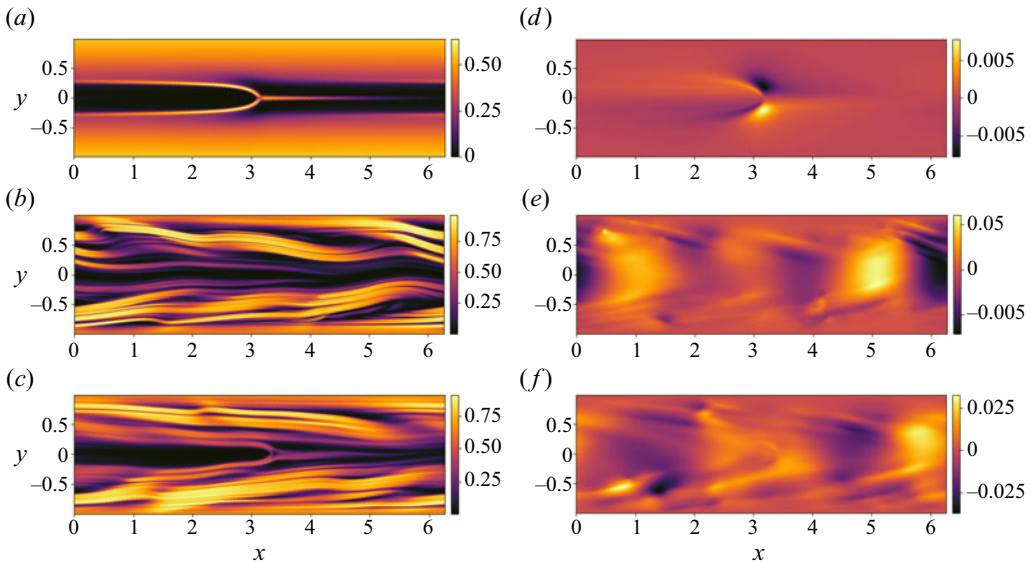
Figure 1. Example snapshots of $\mathrm{tr}(\boldsymbol{C})/L_{max}^2$ and vertical velocity v for the states initially explored in Dubief *et al.* (2022). (*a,d*) Steady arrowhead regime at $Re = 1000$, $Wi = 50$, $\beta = 0.9$, $L_{max} = 90$, $Sc = 500$; (*b,e*) EIT at $Re = 1000$, $Wi = 50$, $\beta = 0.9$, $L_{max} = 70$, $Sc = 500$; (*c,f*) CAR at $Re = 1000$, $Wi = 50$, $\beta = 0.9$, $L_{max} = 70$, $Sc = 500$. We show that these state do not succeed each other but coexist in parameter space.

an intermittent arrowhead (IAR) that we now believe is actually a weaker version of CAR and not a distinct state.

Examples of the three non-trivial attractors are reported in figure 1, where we show contours of the polymer trace $\mathrm{tr}(\boldsymbol{C})/L_{max}^2$. The SAR state features a pair of symmetric sheets of polymer extension, which sit close to the channel centreline, bending to meet at $y = 0$. A highly stretched central sheet then extends downstream along the centreline for almost half of the computational domain. Both EIT and CAR show intense polymer stretch in near-wall regions, with many wavy sheets of polymer extension layered on top of one another. The states are visually very similar, though CAR features a weak, distorted arrowhead structure near the centre of the domain.

We trigger each of the states discussed above and shown in figure 1 by time stepping appropriate initial conditions. The SAR attractor was initially found via nonlinear saturation of the linear centre mode instability as described in Page *et al.* (2020). We found the SAR to always be stable, and were able to obtain this state at other parameter settings by supplying a converged arrowhead obtained nearby in parameter space as an initial condition. We triggered the chaotic states CAR and EIT by applying blowing and suction at the wall, starting from either SAR (to obtain CAR) or the L state (to obtain EIT). The blowing and suction is similar to that used in previous studies (Dubief *et al.* 2013; Samanta *et al.* 2013) and takes the form

$$v(y = \pm 1) = \mp A \sin(2\pi x/L_x), \tag{2.8}$$

with $A = 2 \times 10^{-3}$. The forcing is active for $0 \le t < 3$. Perturbations from the wall were found to be necessary to trigger the self-sustained chaotic states. In contrast, arbitrary perturbations applied in the core of the domain did not trigger chaotic behaviour.
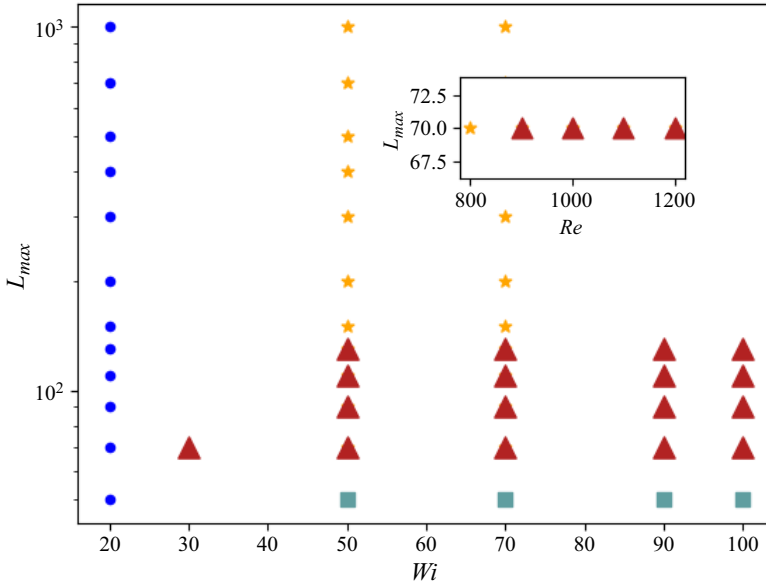
Figure 2. Summary of computations and the attractors found over the parameter space. Blue circles indicate that only the L state was found as an attractor, orange stars indicate that the SAR and L coexist as attractors, light blue squares indicate that L and EIT coexist as attractors and red triangles indicate that L, EIT, SAR and CAR all coexist as attractors. For the main plot, $Sc = 500$, $\beta = 0.9$ and $Re = 1000$ while for the inset $Wi = 50$, $\beta = 0.9$ and $Sc = 500$ again. At $L_{max} = 50$ only EIT and L were explored as attractors as SAR/CAR become prohibitively expensive computationally.

3. Multistability of two-dimensional viscoelastic channels

In this section we summarise our computations and map out regions of multistability. We also explore the impact of changing the flow parameters on the appearance and statistical properties of the various attractors.

3.1. *Coexistence of attractors in parameter space*

The parameter space here is five dimensional and so a systematic search was impractical. However, a preliminary investigation indicated that Wi and L_{max} were the most important parameters (yielding the most qualitative changes) so they were the focus of the search; see figure 2. Over the range $(Wi, L_{max}) \in [20, 70] \times [50, 1000]$ at $Sc = 500$, $\beta = 0.9$ and $Re = 1000$, the L state is linearly stable. This is consistent with the centre-mode instability appearing at slightly higher Wi (see figure 2 in Page *et al.* (2020) where $Sc = 1000$ was used). However, the consequence of the centre-mode instability – the SAR state – is seen at lower Wi as the instability is subcritical. The SAR state was found to be an attractor for $L_{max} \geq 70$ and $Wi \geq 30$ consistent with Page *et al.* (2020). Interestingly, the CAR was only found where SAR also exists and is stable (basically for $Wi \geq 50$ and $L_{max} \in [70, 120]$) excluding the possibility of a SAR-to-CAR bifurcation in this (Wi, L_{max}) range. Elasto-inertial turbulence was found for $Wi \in [30, 100]$, $L_{max} \in [50, 130]$ with $\beta \in [0.9, 0.97]$, $Re \in [900, 1200]$ and $Sc \geq 500$. In terms of figure 2, CAR and EIT coexist when L_{max} is as low as 50 where only EIT and the L state were simulated. Attempts to simulate SAR and CAR for this value of L_{max} were prohibitively expensive computationally due to the loss of positive definiteness and the high spatio-temporal resolution required.

The general conclusion from figure 2 is that the nonlinear states first reported in Dubief *et al.* (2022) – SAR, CAR and EIT – coexist in parameter space rather than succeeding each other as attractors. The latter scenario would suggest dynamical connections between the states in which one loses stability to another, but this seems not to be the case at least in the parameter ranges considered. The fact that SAR and CAR coexist as attractors for the parameters considered is particularly surprising as CAR plausibly looks like the indirect result of a bifurcation off SAR.

3.2. *Distinguishing between CAR and EIT*

Figure 1 shows that the CAR and EIT states look very similar and developing some quantitative measure to distinguish them is important. Another issue is whether either state is just a long-lived transient. For example, does CAR eventually evolve into the EIT state? This latter question is impossible to answer definitively with finite-time computations but what can be said is that over the course of our simulations (some of duration over 1000 h/U_b), CAR never collapsed.

The defining feature of CAR is the mixture of an arrowhead structure at the midplane with the chaotic stretched polymer sheets towards the walls that characterise EIT. A quantity well suited to picking the former feature out is

$$C_{grad} := \frac{1}{L_x} \int |\partial_x C'_{kk}(x, y = 0)| \, \mathrm{d}x, \tag{3.1}$$

which is the streamwise-averaged gradient magnitude of the perturbation over the L state trace along the centreline. We also use the L_2 norm of the velocity difference from the laminar flow – a turbulent kinetic energy

$$\mathrm{TKE}_L := \frac{1}{2L_x} \int_{\Omega} (\boldsymbol{u} - \boldsymbol{u}_L)^2 \, \mathrm{d}\Omega, \tag{3.2}$$

to compare CAR and EIT. Figure 3(*a*) shows the two-dimensional probability density function over these two quantities for the CAR and EIT states collected over a 1000 h/U_b time period. The turbulent kinetic energy of EIT and CAR are very similar but, as expected, C_{grad} is much larger for CAR than EIT.

Another differentiator between EIT and CAR is the result of projecting onto the eigenmodes of the symmetric centre mode (CM) and the antisymmetric TS mode as

$$\langle \phi_j^{\dagger}, \phi \rangle = \frac{1}{2} \int_{-1}^{1} \phi_j^{\dagger *} \phi \, \mathrm{d}y, \tag{3.3}$$

with

$$\phi(y) := \frac{1}{L_x} \int_0^{L_x} \varphi(x, y) \mathrm{e}^{\mathrm{i}x} \, \mathrm{d}x, \tag{3.4}$$

where $j = \{\text{CM, TS}\}$, $\varphi = [u', v', p', C'_{xx}, C'_{yy}, C'_{zz}, C'_{xy}]$ is the perturbation to the L state and ϕ denotes the projection onto the $k_x = 1$ mode (* denotes complex conjugate and $\dagger$ the adjoint). Figure 3(*b*) shows that this projection for the same perturbation trajectories used in figure 3(*a*) produces the same desired separation. The projection onto the centre mode is much larger than the TS mode one for both chaotic states. This is caused by the fact that the trace of the conformation tensor C in the TS eigenmodes has a much larger amplitude than the other components, but its spatial extension is significantly smaller; see figure 3(*c,d*).
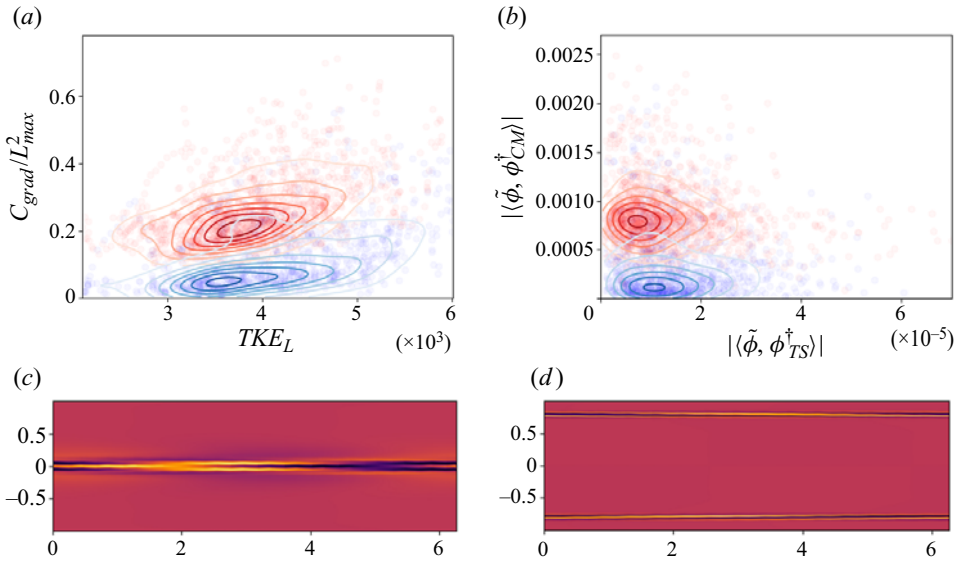
Figure 3. (*a*) Plot of C_{grad}/L_{max}^2 vs TKE_L as defined in the main text for EIT (blue) and CAR (red) identified at $Re = 1000$, $Wi = 50$, $L_{max} = 70$, $\beta = 0.9$, $Sc = 500$ for a finite-time interval $T \approx 1000$; (*b*) projection of the same EIT trajectory (blue) and CAR (red) onto the TS mode versus the projection onto the centre mode. Contours represent the two-dimensional probability density function (p.d.f.) over the two quantities indicated by the figure axes. The figures present observables to show that EIT and CAR are two separate attractors; (*c*) tr(C) of the centre mode for the aforementioned parameters and $k_x = 1$. (*d*) *Idem* for the TS mode that becomes unstable at sufficiently large Re. The shown eigenmodes have arbitrary amplitude. Note that the projection of the TS mode is much smaller than that of the centre mode due to the smaller spatial extension of tr(C), which is the largest term in the corresponding eigenmode.

3.3. *Effect of varying Wi and L_{max}*

The kinetic energy of the SAR increases for increasing L_{max}, in line with the results previously reported (Buza *et al.* 2022*a*; Dubief *et al.* 2022). Figure 4(*a*) shows the time series of the volume-averaged trace for CAR corresponding to $L_{max} = \{70, 90, 110\}$ at $(Wi, Re, Sc, \beta) = (50, 1000, 500, 0.9)$ and $L_{max} = 130$ at $(Wi, Re, Sc, \beta) = (50, 1000, 1000, 0.9)$ where the change in Sc was necessary to maintain chaotic dynamics (ditto for the corresponding SAR). The figure shows that the CAR states undergo periods of calmer, less energetic dynamics alternating with more active periods. The duration of the calmer events increases with L_{max} as shown by the increasing distance between peaks of the time series. This behaviour indicates a continuous transition between the previously reported CAR and intermittent arrowhead regimes, leading to the conclusion that these states are two ends of the same attractor, hereafter labelled CAR. The IAR discussed in Dubief *et al.* (2022) is simply a CAR state where the calm phases dominate the chaotic dynamics that occurs as L_{max} gets large for example.

The effect of varying L_{max} on the EIT states can be seen in figure 5 where the length scales in instantaneous snapshots increase with L_{max}. This is further supported by considering tr(C) at any arbitrary horizontal line ($y = -0.6$ in this case), which is shown in figure 5(*d*) and its Fourier transform in figure 5(*e*). The latter figure shows that for increasing L_{max}, the energy content in the larger scales (smaller wavenumbers) is increased.

The effect of increasing Wi on the EIT state is to make the polymer sheets more undulating spatially and temporally; see figure 6. Increasing Wi also intensifies the
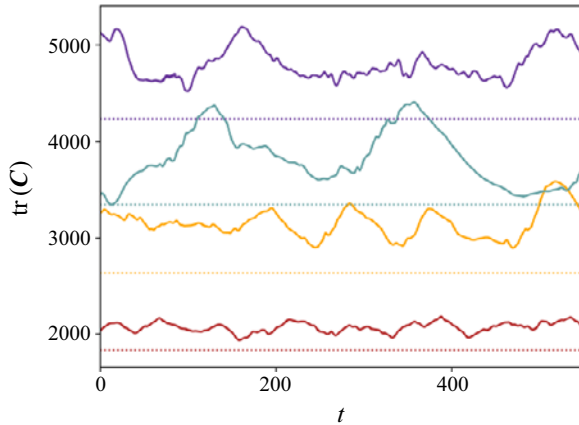
Figure 4. (*a*) Time series corresponding to several CARs (solid) and the corresponding SAR (dashed) at $Re = 1000$, $Wi = 50$, $\beta = 0.9$ with $Sc = 500$ for $L_{max} = \{110, 90, 70\}$ (second top to bottom) and $Sc = 1000$ for $L_{max} = 130$ (top). The figure shows how the duration of the calm–active phases becomes longer with increasing L_{max}, i.e. the peaks of tr(C) become more separated in time. This shows that the IAR and CAR reported in Dubief *et al.* (2022) are smoothly connected and so correspond to the same attractor.
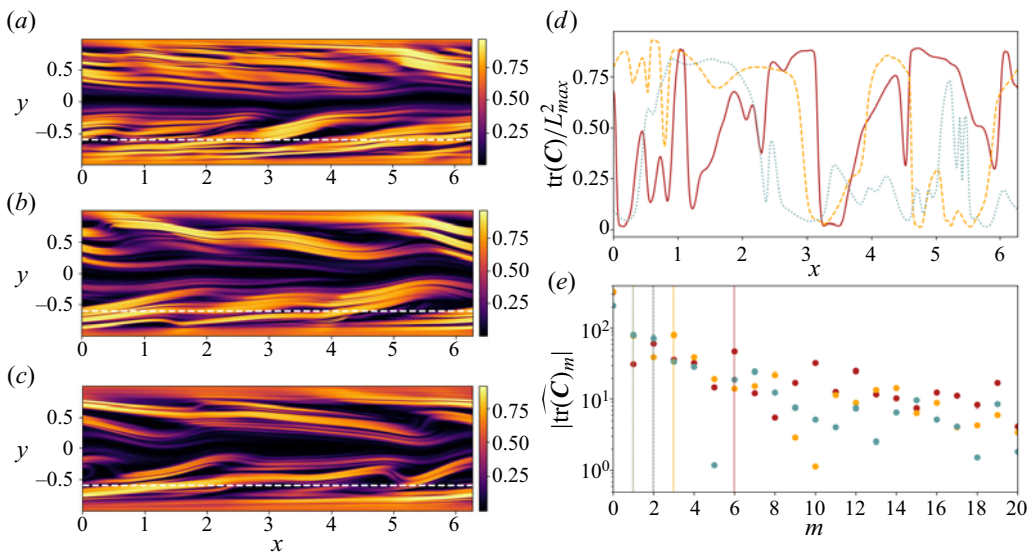

Figure 5. (*a–c*) Snapshots of tr(C)/L_{max}^2 of EIT with varying L_{max} for fixed $Re = 1000$, $Wi = 50$, $\beta = 0.9$, (*a*) $L_{max} = 50$, (*b*) $L_{max} = 70$, (*c*) $L_{max} = 90$ and $Sc = 500$ for all cases. (*d*) Plot showing tr(C)/L_{max}^2 along the arbitrarily chosen line $y = -0.6$ for $L_{max} = 50$ (red), $L_{max} = 70$ (orange), $L_{max} = 90$ (blue). (*e*) Fourier transform of L_{max} for the lines in the top right figure illustrating how the length scales in the flow increase with L_{max}, i.e. smaller L_{max} shows greater amplitudes in the lower wavenumber modes. The vertical lines indicate the wavenumbers corresponding to the two smallest wavenumbers (apart from 0) for each L_{max} above.

polymer layers that reach closer to the centreline. The same trends were also observed for decreasing L_{max} and are found also for the CAR state. A discussion about the evolution of the SAR states with Wi can be found in Buza *et al.* (2022*a*).
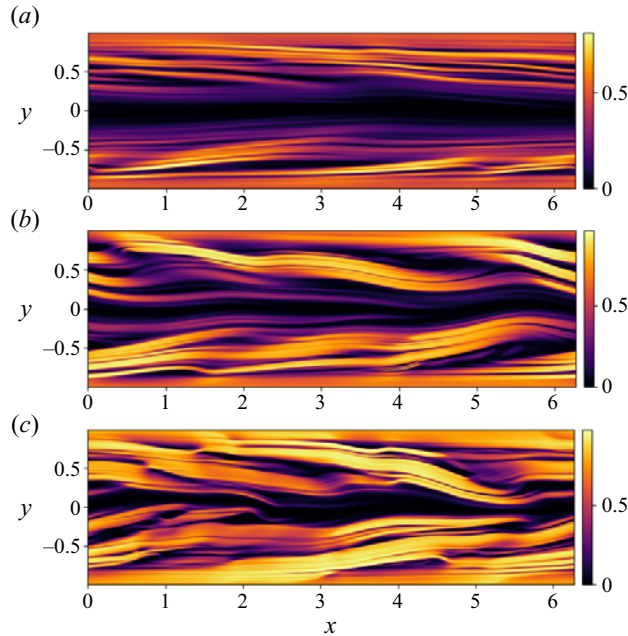
Figure 6. Snapshots of $\mathrm{tr}(C)/L_{max}^2$ of EIT with varying *Wi* for fixed $Re = 1000$, $L_{max} = 70$, $\beta = 0.9$, $Sc = 500$. Results are shown for (*a*) $Wi = 30$, (*b*) $Wi = 50$, (*c*) $Wi = 100$.

3.4. *Effect of varying Re, β and Sc*

Elasto-inertial turbulence and CAR remain robust as the Reynolds number is increased away from where they first appear in parameter space. As an example, figure 7(*b*,*d*,*f*) shows the CAR for three different $Re = \{900, 1100, 1200\}$, while keeping the remaining parameters fixed. The intensity of the dynamics increases while the arrowhead persists at the centreline, consistent with Dubief *et al.* (2022).

Increasing the polymer concentration, β, also intensifies the chaotic dynamics present. Figure 7(*a*,*c*,*e*) shows CAR for $\beta = \{0.9, 0.95, 0.97\}$ for fixed $Re = 1000$, $Wi = 50$, $L_{max} = 70$, and $Sc = 500$. A larger β leads to more active chaotic dynamics. Steady arrowhead states have been observed at values as low as $\beta \approx 0.5$ (Buza *et al.* 2022*a*; Dubief *et al.* 2022; Morozov 2022), whereas we have found that chaotic states (EIT and CAR) cannot be sustained for values below $\beta \approx 0.8$ (using $Re = 1000$, $L_{max} = 70$, $Wi = 50$ and $Sc = 500$).

The majority of the results presented here were computed using $Sc = 500$ as a compromise between including a vanishingly small real diffusion (see, e.g. El-Kareh & Leal 1989) and enough diffusion to numerically stabilise the time-stepping spectral code at the resolutions used. The value of $Sc = 500$ was also selected as the best match to the previous finite-difference computations reported in Dubief *et al.* (2022) and Page *et al.* (2020) where a value of $Sc = 1000$ was taken (finite-difference codes already have some implicit numerical diffusion so less needs to be added explicitly to stabilise time stepping compared with a spectral code). Even then, the EIT reported in figure 2 of Page *et al.* (2020) (the red square at $Wi = 20$, $\beta = 0.9$, $L_{max} = 500$ and $Re = 1000$) could only be recovered by using neighbouring parameter values $Wi = 30$, $\beta = 0.9$, $L_{max} = 120$ and $Re = 1000$. Runs were also carried out with $Sc = 150$ and 1000 that confirmed that all four states (EIT, CAR, SAR and L) as well as their coexistence are robust. The exact parameter
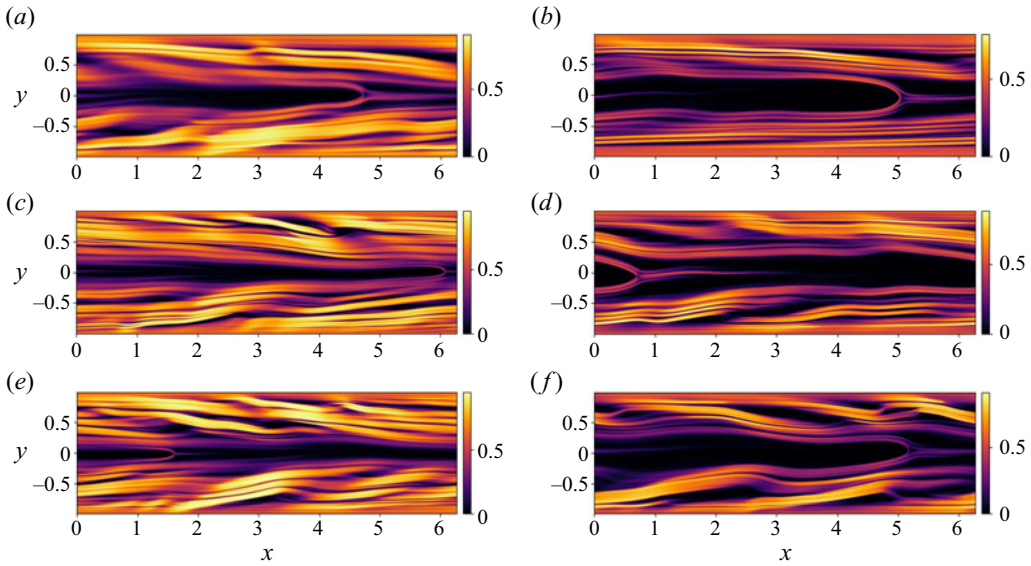
981 A30-10

Figure 7. (*a,c,e*) Snapshots of tr(C)/L_{max}^2 for CAR with varying β at $Re = 1000$, $Wi = 50$, $L_{max} = 70$ and $Sc = 500$: (*a*) $\beta = 0.9$, (*c*) $\beta = 0.95$, (*e*) $\beta = 0.97$. (*b,d,f*) Snapshots of tr(C)/L_{max}^2 for CAR with varying Re at $Wi = 50$, $L_{max} = 120$, $\beta = 0.9$ and $Sc = 500$: (*b*) $Re = 900$, (*d*) $Re = 1100$, (*f*) $Re = 1200$. Increasing β and Re separately or together intensifies the chaotic dynamics in agreement with Dubief *et al.* (2022).

limits for their coexistence, however, do depend on Sc and taking $Sc \leq 50$ killed the chaotic states.

4. Dynamic connections between attractors

The goal of this section is to explore how the various attractors – L, SAR, CAR and EIT – are organised in state space. Of primary concern is identifying which states share basin boundaries and which do not. The physical features present in the different states, such as the presence of a polymer sheet across the midplane or the undulations of polymer sheets closer to the wall, are common to several of the states identified. It is therefore natural to ask how transitions can occur between them and how they come into existence as the parameters are varied.

As an initial check, we first examined the linear stability of the SAR state that results from the centre-mode instability found by Garg *et al.* (2018) in a pipe and Khalid *et al.* (2021*a*) in a channel. This bifurcation is generally subcritical in both Re and Wi (Wan *et al.* 2021; Buza *et al.* 2022*b*) with the SAR solution emerging as the upper branch solution (Page *et al.* 2020; Buza *et al.* 2022*a*; Morozov 2022). We examined the two-dimensional linear stability of the SAR states performing a global stability analysis using an implicitly restarted Arnoldi method (Sorensen 1992; Bagheri *et al.* 2009). The linear stability analysis was carried out in the frame travelling with the speed of the SAR, where the state corresponds to a fixed point (the perturbation was represented by $N_x = 64$ streamwise and $N_y = 512$ wall-normal modes). A subset of SAR states coexisting with EIT/CAR were tested and found to be linearly stable to two-dimensional perturbations consistent with the time-stepping numerics. Interestingly, while this work was being performed, another group found that the SAR state is, however, linearly unstable to three-dimensional perturbations
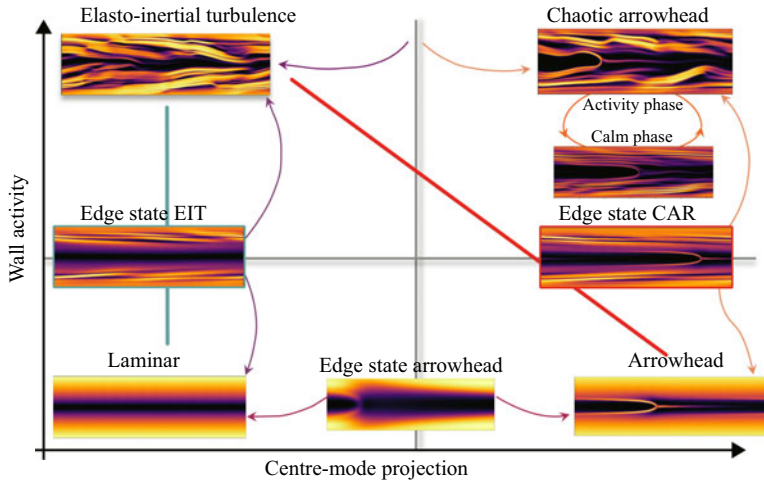
Figure 8. Sketch of the state space configuration. The four quadrants represent the basins of attraction corresponding to the states EIT, CAR, SAR, L. The solid lines emanating from the states represent trajectories approaching and departing different regions of the state space. The thick lines indicate the edge tracking carried out: between EIT and L (blue), between EIT and SAR (red) (see figure 9). The edge states resulting from the bisection algorithm are framed with the same colour. The chaotic attractors undergo calm and active phases (see figure 4) and approach the edge states during the calm phase.

where there is a non-vanishing spanwise wavenumber (Lellep, Linkmann & Morozov 2023).

As the L state is also linearly stable over the parameter space being considered, the transition between the SAR, L and the other chaotic states must then be through finite-amplitude perturbations. To shed some light on this, the saddle states lying in the boundaries between the basins of attraction of the aforementioned attractors, i.e. the edge states, are considered below.

4.1. *Edge states*

Edge states are attracting states on the edge manifold, a codimension one manifold lying in the boundary between different basins of attraction. Edge states are thus helpful to shed light on the global structure of the state space (Schneider & Eckhardt 2006; Skufca, Yorke & Eckhardt 2006; Duguet, Willis & Kerswell 2008). These states can be identified by the so-called classical edge tracking algorithm based on threshold attainment of a key observable of the flow (Itano & Toh 2001; Skufca *et al.* 2006).

The choice of an observable to uniquely label trajectories as lying within a certain basin of attraction is not straightforward in viscoelastic flows as discussed above in § 3.2. The choice used here is the L_2 norm of the vertical velocity, $\|v\|^2$, which is zero for the L state. Edge tracking was then performed between (i) EIT and L (shown in figure 8 as a blue line) and (ii) EIT and SAR (shown in figure 8 as a red line). The use of $\|v\|^2$ – as well as other observables based on $\mathrm{tr}(C)$ – was not able to uniquely distinguish between trajectories belonging to CAR or to EIT at every instant, as illustrated in figure 3. The existence of an edge manifold between CAR and EIT can still be explored by probing the state space with specific trajectories and assessing whether an arrowhead structure survives or not after a sufficiently long time but this is a laborious process.

The simplest edge state identified is the 'lower branch' unstable SAR between the 'upper branch' stable SAR and L (Buza *et al.* 2022a). Figure 9(*a*) shows the time series of the
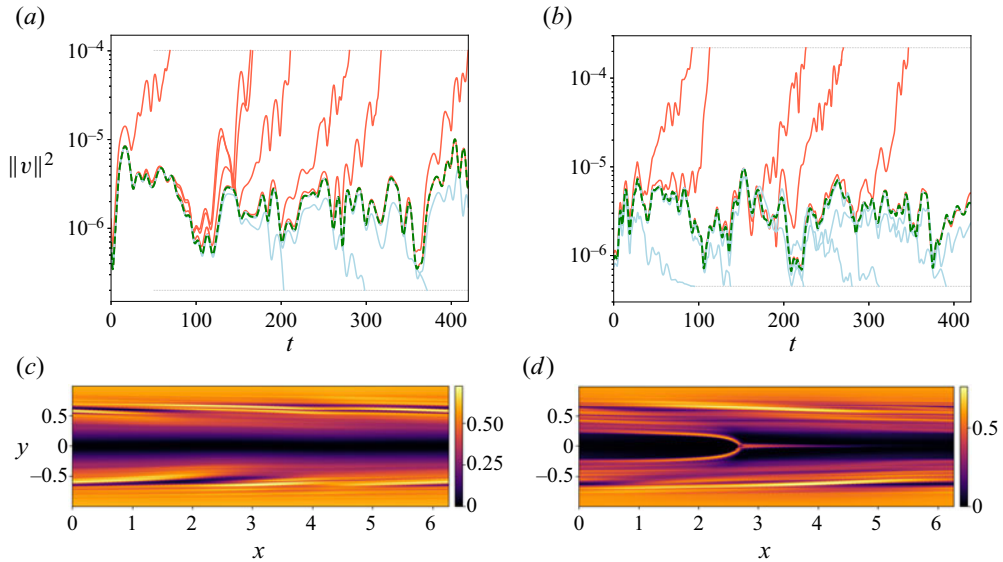
Figure 9. Top edge tracking for $Re = 1000$, $Wi = 50$, $\beta = 0.9$, $L_{max} = 70$, $Sc = 500$: (*a*) between EIT and L (the green edge trajectory is bracketed by red trajectories approaching EIT and blue trajectories relaminarising to L), and (*b*) between EIT and SAR (the green edge trajectory is bracketed by red trajectories approaching CAR instead of EIT and blue trajectories approaching SAR). Bottom: (*c*) snapshot of $\mathrm{tr}(C)/L_{max}^2$ of the edge trajectory in (*a*) at $t = 400$ that shows a strong polymer layer at $y \approx \pm[0.75, 0.85]$. Plot (*d*) repeats this for (*b*). The red line in figure 8 explains how it is possible to reach the CAR edge state starting from a bisection between EIT and SAR.

edge tracking between EIT and L and figure 9(*c*) shows a snapshot of this trajectory, a weakly chaotic state characterised by polymer layers located at $y \approx \pm[0.75, 0.85]$. The edge state reveals the significance of the polymer layers located close to the walls, as they are responsible for the self-sustained chaotic dynamics within the edge. Furthermore, these layers have been observed during the calm phases of both EIT and CAR, suggesting that they related to the driving mechanism for EIT. The edge state between CAR and L can be compared with the edge state found between EIT and SAR, figure 9(*b,d*), which also corresponds to a weakly chaotic state characterised by polymer layers located at $y \pm [0.75, 0.85]$ with the presence of an arrowhead structure in the centre of the channel.

The results of the edge tracking suggest an organisation of state space sketched in figure 8 over a two-dimensional plane of wall activity against centre-mode projection. Here each state is shown within its basin of attraction and the chaotic states are shown approaching their corresponding edge states in their calm phases. Our calculations suggest that there could be an intersection between the basins of attraction of EIT, CAR, SAR and L but the saddle state residing here is not computable using bisection since it must have two unstable directions.

4.2. *Kinetic-to-elastic energy transfer*

Our calculations of chaotic states highlight the importance of polymer activity at the walls. Here we identify the key location where kinetic energy is transferred to elastic polymer energy. The energy transfer flux from the perturbation kinetic energy to the perturbation
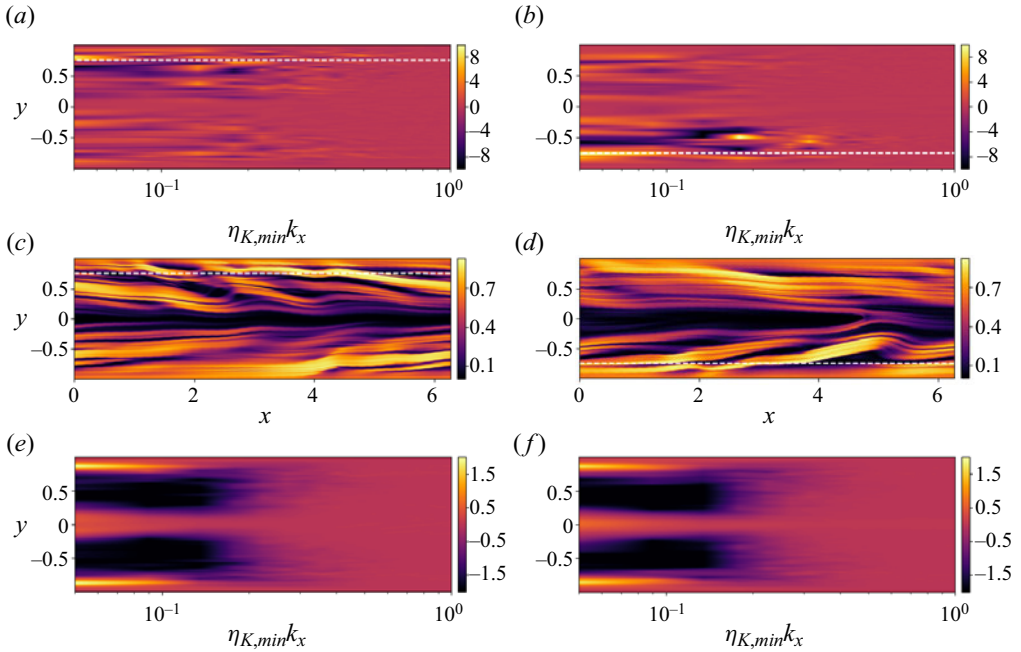
Figure 10. (*a*) Cospectra between the perturbation kinetic energy to the perturbation elastic energy for EIT at $Re = 1000$, $Wi = 50$, $\beta = 0.9$, $L_{max} = 70$, $Sc = 500$ as a function of the wall-normal coordinate y just before an active phase. The streamwise wavenumber k_x is normalised with the minimum mean Kolmogorov length scale. The white dashed line is at $y = 0.75$. (*c*) Instantaneous snapshots of $\text{tr}(C)/L_{max}^2$ corresponding to the cospectra in (*a*). (*b*) Same as (*a*) but for snapshots of CAR at the same parameters. (*d*) Instantaneous snapshot of $\text{tr}(C)/L_{max}^2$ corresponding to the cospectra in (*b*). (*e*) Mean cospectra for same EIT as (*a*). (*f*) *Idem* for CAR in (*b*). The figure illustrates how the energy exchange ahead of an active phase occurs at polymer layers located at $y \approx \pm[0.75, 0.85]$.

elastic energy is

$$\Pi_e' := \frac{1 - \beta}{Re} T_{ij}' S_{ij}' \tag{4.1}$$

(e.g. see equations (9)–(12) in Dubief *et al.* 2022), where primed variables indicate perturbations from the mean turbulent state, and the dissipation rate of TKE, $\varepsilon := (\beta/Re)\partial_j u_i' \partial_j u_i'$, defines the Kolmogorov length scale,

$$\eta_K := \left[\frac{(\beta/Re)^3}{\bar{\varepsilon}} \right]^{1/4}, \tag{4.2}$$

where η_K is defined for classic turbulence. Although η_K might seem to depend on β at first glance, the definition of Re is based on the total viscosity η.

Figure 10 shows the instantaneous cospectra of Π_e' and the corresponding instantaneous field of $\text{tr}(C)/L_{max}^2$ for each of EIT and CAR when they are on the verge of a high-activity phase. These cospectra highlight that as the trajectories depart from their calm phases, the largest rate of energy exchange from the kinetic energy to the elastic energy, i.e. maximal Π_e', takes place at a location $y \approx [0.75, 0.85]$ in (*a*) and $y \approx [-0.75, -0.85]$ in (*b*). Notably, the critical layer for the stable TS waves for $Re = 1000$, $Wi = 50$, $\beta = 0.9$, $L_{max} = 70$, $Sc = 500$ can be found at $y \approx \pm 0.79$. This corresponds to the location of the polymer layers harvesting kinetic energy to build

981 A30-14

self-sustained chaotic dynamics. The importance of the critical layer in supporting chaotic dynamics has been previously discussed in the transition route to EIT based on viscoelastic TS waves (Shekar *et al.* 2019, 2020, 2021). It is also interesting to note that the main exchange from elastic energy to kinetic energy happens in the dark regions of figure 10. As can be observed throughout the various figures in this work, this region supports the larger-scale motions during the observed self-sustained chaotic process. Moreover, these polymer sheets experience the same kind of undulation for the edge states as for the complex chaotic attractors when departing from the calm phases. The time-averaged cospectra (shown in figure 10*e*,*f*) confirm the importance of the energy exchange in the neighbourhood of the wall $y \approx [0.75, 0.85]$. As expected, the time-averaged cospectra for EIT and CAR are very similar as the main energy exchange driving the chaotic dynamics is located in the same region (Dubief *et al.* 2022).

5. Discussion

In this paper we have carried out a suite of two-dimensional simulations of viscoelastic channel flow to explore where the various states described in Dubief *et al.* (2022) exist in (Wi, Re, β, L_{max}, Sc) parameter space. A fully spectral code using the FENE-P model has been used to confirm the existence of four distinct states: the L state, SAR, CAR and EIT, EIT (the intermediate arrowhead state, IAR, of Dubief *et al.* (2022) has been clarified as a CAR where calm periods dominate over the chaotic dynamics). Elasto-inertial turbulence has been found for (Wi, Re, β, L_{max}, Sc) $\in$ [30, 100] $\times$ [900, 1200] $\times$ [0.9, 0.97] $\times$ [50, 130] $\times$ [500, ∞) with increasing Wi, Re and β and decreasing L_{max} intensifying the chaotic behaviour. Small Sc values of ≈ 50 suppress the chaotic dynamics, while larger values of Sc allow the chaos to exist in a greater region of parameter space.

The most significant finding, however, is that there is a substantial set of parameter values (shown in figure 2) where all four states coexist as attractors. This contrasts with the classic 'supercritical' scenario where a succession of unique attractors appear of increasing complexity as parameters are changed to make the flow more unstable (e.g. increasing Wi or decreasing L_{max}). In particular, no evidence has been found that a bifurcation off the SAR leads ultimately to either CAR or EIT (at least in two dimensions) as hypothesized after the recent discovery of the centre-mode instability (see, e.g. Garg *et al.* 2018; Page *et al.* 2020; Khalid *et al.* 2021*a*; Datta *et al.* 2022; Shankar & Subramanian 2022). It may well be that such a subcritical bifurcation sequence exists at, for example, higher Wi or lower L_{max} beyond the region of multistability. Our results do not go high enough in Wi nor low enough in L_{max} to see this. In terms of polymer concentration, SAR has been found as low as $\beta = 0.5$ but remains stable even when chaotic dynamics emerges for $\beta \geq 0.9$.

To further probe the connection between the various states, various edge states were identified between pairs of attractors, and used to sketch the relative locations of the states in phase space. As expected, the edge state between SAR and L is the unstable 'lower branch' SAR found in Buza *et al.* (2022*b*,*a*) while the edge states between CAR and L, and between EIT and SAR correspond to weakly chaotic states. The chaotic edge states reveal the presence of unstable polymer layers at $y \approx \pm[0.75, 0.85]$, qualitatively similar to the edge states between CAR and L, and between EIT and SAR. By examining the energy transfer flux, these near-wall polymer layers were found to be where the dominant energy transfer occurs from the velocity field to the polymers that seems fundamental for the self-sustained chaotic dynamics. In contrast, the chaotic flow appeared to be insensitive to the arrowhead structure populating the centreline region. This then further suggests

that the chaotic dynamics is not related to the centre-mode instability or its arrowhead manifestation but is more a wall-focused phenomenon.

The conclusion of the present study is then that the two-dimensional linear instability discovered by Garg *et al.* (2018) in pipe flow and Khalid *et al.* (2021*a*) in a channel, and the resulting arrowhead structure (Page *et al.* 2020; Buza *et al.* 2022*a*; Morozov 2022), appear dynamically disconnected from EIT at least in the two dimensions studied here. Instead, our study suggests that to trigger any chaotic motion, it is necessary to excite polymer layers located at $y \approx \pm[0.75, 0.85]$ from the wall. Recent work discussing viscoelastic TS waves (Shekar *et al.* 2020, 2021) suggests a plausible mechanism as polymer stretch is found localised at the near-wall critical layer of the TS waves. A three-dimensional route to EIT stemming from the arrowhead cannot be ruled out. Lellep *et al.* (2023) have shown that three-dimensional perturbations render the arrowhead linearly unstable and a possible route to EIT should be explored in this scenario. Another possibility is the very recent discovery of a wall-localised linear instability (Beneitez, Page & Kerswell 2023). Clearly, further efforts are needed to untangle the mechanism leading to EIT but now this can be focused on near-wall processes or three-dimensional alternatives.

Declaration of interests. The authors report no conflict of interest.

Author ORCIDs.

- Miguel Beneitez https://orcid.org/0000-0002-4045-7262;
- Jacob Page https://orcid.org/0000-0002-4564-5086;
- Yves Dubief https://orcid.org/0000-0001-8181-7597;
- Rich R. Kerswell https://orcid.org/0000-0001-5460-5337.

REFERENCES

BAGHERI, S., ÅKERVIK, E., BRANDT, L. & HENNINGSON, D.S. 2009 Matrix-free methods for the stability and control of boundary layers. *AIAA J.* **47** (5), 1057–1068.

BENEITEZ, M., PAGE, J. & KERSWELL, R.R. 2023 Polymer diffusive instability leading to elastic turbulence in plane Couette flow. *Phys. Rev. Fluids* **8**, L101901.

BURNS, K.J., VASIL, G.M., OISHI, J.S., LECOANET, D. & BROWN, B.P. 2020 Dedalus: a flexible framework for numerical simulations with spectral methods. *Phys. Rev. Res.* **2** (2), 023068.

BUZA, G., BENEITEZ, M., PAGE, J. & KERSWELL, R.R. 2022*a* Finite-amplitude elastic waves in viscoelastic channel flow from large to zero Reynolds number. *J. Fluid Mech.* **951**, A3.

BUZA, G., PAGE, J. & KERSWELL, R.R. 2022*b* Weakly nonlinear analysis of the viscoelastic instability in channel flow for finite and vanishing Reynolds numbers. *J. Fluid Mech.* **940**, A11.

CHANDRA, B., SHANKAR, V. & DAS, D. 2018 Onset of transition in the flow of polymer solutions through microtubes. *J. Fluid Mech.* **844**, 1052–1083.

CHOUEIRI, G.H., LOPEZ, J.M. & HOF, B. 2018 Exceeding the asymptotic limit of polymer drag reduction. *Phys. Rev. Lett.* **120** (12), 124501.

CHOUEIRI, G.H., LOPEZ, J.M., VARSHNEY, A., SANKAR, S. & HOF, B. 2021 Experimental observation of the origin and structure of elastoinertial turbulence. *Proc. Natl Acad. Sci. USA* **118** (45), e2102350118.

DATTA, S.S., *et al.* 2022 Perspectives on viscoelastic flow instabilities and elastic turbulence. *Phys. Rev. Fluids* **7** (8), 080701.

DRAAD, A.A., KUIKEN, G.D.C. & NIEUWSTADT, F.T.M. 1998 Laminar–turbulent transition in pipe flow for Newtonian and non-Newtonian fluids. *J. Fluid Mech.* **377**, 267–312.

DUBIEF, Y., PAGE, J., KERSWELL, R.R., TERRAPON, V.E. & STEINBERG, V. 2022 First coherent structure in elasto-inertial turbulence. *Phys. Rev. Fluids* **7** (7), 073301.

DUBIEF, Y., TERRAPON, V.E. & HOF, B. 2023 Elasto-inertial turbulence. *Annu. Rev. Fluid Mech.* **55**, 675–705.

DUBIEF, Y., TERRAPON, V.E. & SORIA, J. 2013 On the mechanism of elasto-inertial turbulence. *Phys. Fluids* **25** (11), 110817.

DUGUET, Y., WILLIS, A.P. & KERSWELL, R.R. 2008 Transition in pipe flow: the saddle structure on the boundary of turbulence. *J. Fluid Mech.* **613**, 255–274.

EL-KAREH, A.W. & LEAL, L.G. 1989 Existence of solutions for all Deborah numbers for a non-Newtonian model modified to include diffusion. *J. Non-Newtonian Fluid Mech.* **33** (3), 257–287.

GARG, P., CHAUDHARY, I., KHALID, M., SHANKAR, V. & SUBRAMANIAN, G. 2018 Viscoelastic pipe flow is linearly unstable. *Phys. Rev. Lett.* **121** (2), 024502.

GOLDSTEIN, R.J., ADRIAN, R.J. & KREID, D.K. 1969 Turbulent and transition pipe flow of dilute aqueous polymer solutions. *Ind. Engng Chem. Fundam.* **8** (3), 498–502.

GROISMAN, A. & STEINBERG, V. 2000 Elastic turbulence in a polymer solution flow. *Nature* **405** (6782), 53–55.

GROISMAN, A. & STEINBERG, V. 2004 Elastic turbulence in curvilinear flows of polymer solutions. *New J. Phys.* **6** (1), 29.

ITANO, T. & TOH, S. 2001 The dynamics of bursting process in wall turbulence. *J. Phys. Soc. Japan* **70** (3), 703–716.

JONES, W.M. & MADDOCK, J.L. 1966 Onset of instabilities and reduction of drag in the flow of relaxing liquids through tubes and porous beds. *Nature* **212** (5060), 388–390.

KHALID, M., CHAUDHARY, I., GARG, P., SHANKAR, V. & SUBRAMANIAN, G. 2021*a* The centre-mode instability of viscoelastic plane Poiseuille flow. *J. Fluid Mech.* **915**, A43.

KHALID, M., SHANKAR, V. & SUBRAMANIAN, G. 2021*b* Continuous pathway between the elasto-inertial and elastic turbulent states in viscoelastic channel flow. *Phys. Rev. Lett.* **127** (13), 134502.

LARSON, R.G., SHAQFEH, E.S.G. & MULLER, S.J. 1990 A purely elastic instability in Taylor–Couette flow. *J. Fluid Mech.* **218**, 573–600.

LELLEP, M., LINKMANN, M. & MOROZOV, A. 2023 Linear stability analysis of purely elastic travelling-wave solutions in pressure-driven channel flows. *J. Fluid Mech.* **959**, R1.

LUMLEY, J.L. 1969 Drag reduction by additives. *Annu. Rev. Fluid Mech.* **1** (1), 367–384.

MEULENBROEK, B., STORM, C., MOROZOV, A.N. & VAN SAARLOOS, W. 2004 Weakly nonlinear subcritical instability of visco-elastic Poiseuille flow. *J. Non-Newtonian Fluid Mech.* **116** (2–3), 235–268.

MOROZOV, A. 2022 Coherent structures in plane channel flow of dilute polymer solutions with vanishing inertia. *Phys. Rev. Lett.* **129** (1), 017801.

MOROZOV, A.N. & VAN SAARLOOS, W. 2007 An introductory essay on subcritical instabilities and the transition to turbulence in visco-elastic parallel shear flows. *Phys. Rep.* **447** (3–6), 112–143.

MYSELS, K.J. 1949 Flow of thickened fluids. U.S. Patent 2492173A.

PAGE, J., DUBIEF, Y. & KERSWELL, R.R. 2020 Exact traveling wave solutions in viscoelastic channel flow. *Phys. Rev. Lett.* **125** (15), 154501.

PAN, L., MOROZOV, A., WAGNER, C. & ARRATIA, P.E. 2013 Nonlinear elastic instability in channel flows at low Reynolds numbers. *Phys. Rev. Lett.* **110** (17), 174502.

SAMANTA, D., DUBIEF, Y., HOLZNER, M., SCHÄFER, C., MOROZOV, A.N., WAGNER, C. & HOF, B. 2013 Elasto-inertial turbulence. *Proc. Natl Acad. Sci. USA* **110** (26), 10557–10562.

SÁNCHEZ, H.A.C., JOVANOVIĆ, M.R., KUMAR, S., MOROZOV, A., SHANKAR, V., SUBRAMANIAN, G. & WILSON, H.J. 2022 Understanding viscoelastic flow instabilities: Oldroyd-B and beyond. *J. Non-Newtonian Fluid Mech.*, 104742.

SCHNEIDER, T.M. & ECKHARDT, B. 2006 Edge of chaos in pipe flow. *Chaos* **16** (4), 041103.

SHANKAR, V. & SUBRAMANIAN, G. 2022 A linear route to elasto-inertial turbulence. *Sci. Talks* **3**, 100051.

SHAQFEH, E.S.G. 1996 Purely elastic instabilities in viscometric flows. *Annu. Rev. Fluid Mech.* **28**, 129–185.

SHEKAR, A., MCMULLEN, R.M., MCKEON, B.J. & GRAHAM, M.D. 2020 Self-sustained elastoinertial Tollmien–Schlichting waves. *J. Fluid Mech.* **897**, A3.

SHEKAR, A., MCMULLEN, R.M., MCKEON, B.J. & GRAHAM, M.D. 2021 Tollmien–Schlichting route to elastoinertial turbulence in channel flow. *Phys. Rev. Fluids* **6** (9), 093301.

SHEKAR, A., MCMULLEN, R.M., WANG, S.-N., MCKEON, B.J. & GRAHAM, M.D. 2019 Critical-layer structures and mechanisms in elastoinertial turbulence. *Phys. Rev. Lett.* **122** (12), 124503.

SID, S., TERRAPON, V.E. & DUBIEF, Y. 2018 Two-dimensional dynamics of elasto-inertial turbulence and its role in polymer drag reduction. *Phys. Rev. Fluids* **3** (1), 011301.

SKUFCA, J.D., YORKE, J.A. & ECKHARDT, B. 2006 Edge of chaos in a parallel shear flow. *Phys. Rev. Lett.* **96** (17), 174101.

SORENSEN, D.C. 1992 Implicit application of polynomial filters in ak-step Arnoldi method. *SIAM J. Matrix Anal. Appl.* **13** (1), 357–385.

SQUIRES, T.M. & QUAKE, S.R. 2005 Microfluidics: fluid physics at the nanoliter scale. *Rev. Mod. Phys.* **77** (3), 977.

TOMS, B.A. 1948 Some observations on the flow of linear polymer solution through straight tubes at high Reynolds number. In *Proceedings International Rheology Congress, Holland*, vol. 2, pp. 135–141. North Holland.

TRAORE, B., CASTELAIN, C. & BURGHELEA, T. 2015 Efficient heat transfer in a regime of elastic turbulence. *J. Non-Newtonian Fluid Mech.* **223**, 62–76.

VARSHNEY, A. & STEINBERG, V. 2018 Drag enhancement and drag reduction in viscoelastic flow. *Phys. Rev. Fluids* **3** (10), 103302.

WAN, D., SUN, G. & ZHANG, M. 2021 Subcritical and supercritical bifurcations in axisymmetric viscoelastic pipe flows. *J. Fluid Mech.* **929**, A16.

WANG, D. & RUUTH, S.J. 2008 Variable step-size implicit-explicit linear multistep methods for time-dependent partial differential equations. *J. Comput. Math.* **26** (6), 838–855.

WHITE, C.M. & MUNGAL, M.G. 2008 Mechanics and prediction of turbulent drag reduction with polymer additives. *Annu. Rev. Fluid Mech.* **40**, 235–256.

ZHANG, M., LASHGARI, I., ZAKI, T.A. & BRANDT, L. 2013 Linear stability analysis of channel flow of viscoelastic Oldroyd-B and FENE-P fluids. *J. Fluid Mech.* **737**, 249–279.

ZHANG, W.-H., ZHANG, H.-N., LI, Y.-K., YU, B. & LI, F.-C. 2021 Role of elasto-inertial turbulence in viscoelastic drag-reducing turbulence. *Phys. Fluids* **33** (8), 081706.

ZHU, L. & XI, L. 2021 Nonasymptotic elastoinertial turbulence for asymptotic drag reduction. *Phys. Rev. Fluids* **6** (1), 014601.